



ARTICLE

Multiple long-range inputs evoke NMDA currents in prefrontal cortex fast-spiking interneurons

Luke Joseph Bogart¹ and Patricio O'Donnell¹

Several aspects of schizophrenia can be mimicked acutely in healthy human volunteers via administration of NMDA glutamate receptor (NMDAR) antagonists. As these agents decrease firing rates in prefrontal cortical (PFC) GABAergic fast-spiking interneurons (FSI) in animal studies, a leading hypothesis on schizophrenia pathophysiology is that NMDAR in FSI are impaired. However, whole-cell recordings of FSI in slices of adult mouse PFC revealed limited amounts of NMDAR-mediated current. Since those studies used local electrical stimulation to activate a heterogeneous set of synaptic inputs to the recorded cell, it is unclear whether specific afferent inputs may preferentially drive NMDAR responses in FSI. Here, we expressed opsins in discrete brain regions projecting to the PFC in adult male mice, enabling light-activation of defined, homogenous sets of long-range inputs to FSI and pyramidal neurons recorded in slices containing medial PFC (mPFC). Stimulation of axons originating from either the contralateral mPFC, ventral hippocampus, or mediodorsal thalamus evoked NMDAR-mediated currents in the vast majority of FSI and in all pyramidal neurons recorded. The observation that multiple long-range inputs to mPFC FSI elicit NMDAR currents suggests that the NMDAR-hypofunction model of schizophrenia may still imply a loss of interneuron inputs, but the sources of reduced excitation may originate from sites upstream of the PFC.

Neuropsychopharmacology (2018) 43:2101–2108; <https://doi.org/10.1038/s41386-018-0029-5>

INTRODUCTION

The prefrontal cortex (PFC) is critical for executive and other cognitive functions, and is considered a central element of pathophysiology underlying schizophrenia [1]. Certain features of schizophrenia can be modeled in healthy human subjects via acute or subchronic administration of non-competing NMDA receptor (NMDAR) antagonists [2], suggesting that altered NMDAR transmission may be involved in disease processes. Following systemic delivery of these drugs to freely behaving animals, *in vivo* recordings of medial PFC (mPFC) neurons have revealed a decrease of firing rates in fast-spiking inhibitory interneurons [3], an observation that provided support to the hypothesis that NMDAR in cortical interneurons are a central site of pathology [1, 4]. Fast-spiking interneurons (FSI) express the calcium-binding protein parvalbumin and provide powerful peri-somatic inhibition to pyramidal neurons that can gate the flow of information into cortex as well as synchronize firing across large numbers of pyramidal neurons [5]. Loss of adequate excitation-inhibition balance can lead to abnormal pyramidal cell (PC) firing and contribute to cognitive and behavioral symptoms of schizophrenia.

While reduced parvalbumin labeling is a highly replicated finding in postmortem brains from schizophrenia patients [1], it is still unclear whether loss of interneuron function can drive or be a consequence of altered excitation-inhibition balance. A critical need to better understand this issue is to determine how NMDAR-mediated synaptic activation of FSI is regulated in health and disease. Rotaru et al. [6] found using slices of adult mouse PFC that AMPA glutamate receptor (AMPA)-mediated currents dominate over NMDAR-mediated currents to a greater degree in FSI than in

PCs. This observation led to questioning the model that NMDAR antagonist-mediated psychotomimetic effects take place by affecting synapses onto FSI, and to some raised doubt about FSI being a primary site of pathology in schizophrenia. That study used local electrical stimulation to recruit axons originating from diverse brain regions that provide a heterogeneous set of inputs to a given PFC neuron, leaving open the question of whether specific inputs may preferentially drive NMDAR responses in FSI in a manner that can be obscured by a nonspecific local electrical stimulation.

Imaging studies of schizophrenia patients have revealed disruptions in connectivity between the PFC and brain regions located upstream, including hippocampus [7–9] and thalamus [10]. Further dissection of these pathways in animal studies has shown that mPFC neurons are contacted by afferents from several long-range sources, including contralateral mPFC [11], ventral hippocampus [12], and mediodorsal thalamus [13], with multiple inputs converging onto individual neurons [14]. However, the relative strength of these inputs to interneurons and their ability to drive synaptic NMDAR responses is not known. Here, we addressed this question by injecting opsins in discrete brain regions projecting to the mPFC in adult mice, enabling input-specific analysis of excitatory synaptic currents in brain slices.

METHODS

In vivo viral-labeling of projections to mPFC
Afferents to mPFC were labeled by stereotaxic injection of adult (≥ 2 months old) male GAD1-EGFP+ mice (JAX #007677, “CB6-Tg(Gad1-EGFP)G42Zjh/J”) with rAAV8-AAV-hSyn-ChrimsonR-

¹Internal Medicine Research Unit, Pfizer Inc., Cambridge, MA 02139, USA

Correspondence: Patricio O'Donnell (Patricio.ODonnell@takeda.com)

Received: 16 November 2017 Revised: 24 January 2018 Accepted: 31 January 2018

Published online: 26 February 2018

2102 tdTomato [15] at the following locations: mPFC (bregma +1.6 mm; X -0.4 mm; Z -2.0 and -1.6 mm, 0.5 μ L/z), unilaterally; ventral hippocampus (bregma -3.4 mm; X \pm 3.35 mm; Z -3.8 and -3.4 mm, 0.5 μ L/z), bilaterally; or mediodorsal thalamus (bregma -1.3 mm; X \pm 0.4 mm; Z -3.6 and -3.3 mm, 0.25 μ L/z), bilaterally, using a 33 gauge Hamilton syringe. Viral vectors were purchased from the University of North Carolina Vector Core and used undiluted at 5.5×10^{12} GC/mL. Animals received sustained-release Meloxicam (4 mg/kg; Wildlife Pharmaceuticals) pre-operatively and buprenorphine (0.1 mg/kg) post-operatively, and all procedures were approved by Pfizer's Institutional Animal Care and Use Committee and were in-line with local regulations. Animals recovered for \geq 4.5 weeks (average of 9 weeks) to allow for expression of ChrimsonR-tdTomato to reach axons projecting to mPFC.

In vitro electrophysiology

Brain slices were prepared using standard procedures [16]. Briefly, mice were anesthetized with isoflurane and perfused intracardially with ice-cold, oxygenated cutting solution (modified artificial cerebrospinal fluid, ACSF, containing, in mM: 125 NaCl, 25 NaHCO₃, 1.25 NaH₂PO₄, 3.5 KCl, 10 glucose, 0.5 CaCl₂, and 3 MgCl₂). Three-hundred-micrometer-thick coronal slices of mPFC were cut in cutting solution on a Leica VT1200S vibratome, and transferred to an incubation chamber containing oxygenated recording solution (ACSF, containing, in mM: 125 NaCl, 25 NaHCO₃, 1.25 NaH₂PO₄, 3.5 KCl, 10 glucose, 2 CaCl₂, and 1 MgCl₂), which was kept in a 34 °C water bath throughout the day. Additional slices containing the injection site were screened under epifluorescence on an electrophysiology rig for labeling of the target brain region by ChrimsonR-tdTomato (Paxinos and Franklin [17]; used as guide for figure labeling), with animals demonstrating mistargeted labeling not being used. Images were acquired in auto-contrast mode using a Hamamatsu Orca-Flash 2.8 camera (model C11440) and Olympus cellSens Dimension v1.14 software. Images were processed to aid visibility of relevant features as indicated in the figure legends. High-power images of ChrimsonR-tdTomato axons had both brightness and contrast increased by 20%, to further aid visibility.

After \geq 45 min recovery from cutting, mPFC-containing slices were transferred to the recording chamber and screened for the presence of tdTomato-labeled axons in infralimbic (IL), prelimbic (PL), and cingulate (CG) cortical areas, all of which were recorded from in this study. Glass micropipettes (4–6 M Ω) were filled with a potassium-gluconate-based internal solution (containing, in mM: 115 K D-gluconate, 10 HEPES, 20 KCl, 2 MgCl₂, 2 MgATP, 2 Na₂ATP, and 0.3 GTP, with 0.125% neurobiotin), and both GFP+ interneurons and non-GFP+ PCs in cortical layers 5 and 6 were targeted for patch-clamp recordings (at 31–33 °C, with oxygenated ACSF superfused at 2 mL/min). Upon break-in, spiking behavior was assessed by injecting current for 500 ms at 50 pA steps ranging from -250 to +400 pA. GFP+ cells responded with classical fast-spiking trains at suprathreshold levels. PCs were classified as putative "type A" or "type B", with the latter lacking the following features present in the former: (1) prominent h-current in response to -250 pA current injection epochs; (2) prominent rebound-depolarization following epoch completion; and (3) after-hyperpolarization following current injection-induced spike trains that overshoot resting potential [11].

Signals were acquired using an Axon Instruments MultiClamp 700B amplifier and Digidata 1550 digitizer, and were low-pass-filtered at 2 kHz during acquisition using Clampex 10.6 software. With the cell voltage clamped at -55 mV, activation through the objective lens of local ChrimsonR-expressing axons in the \times 40 field of view containing the patched cell was achieved by flashing a red light-emitting diode (LED; 615–655 nm emission, 5 ms pulses; RLX module for X-Cite XLED1, Excelitas Technologies Corp.) every 30 s. If the cell exhibited inward current responses at a monosynaptic delay from light onset (\leq 4 ms), picrotoxin was

added to the perfusion solution (10 μ M, "PCX") to block GABA_AR and a stable, subthreshold excitatory postsynaptic current (EPSC) was obtained by titrating LED power. Responses continued to be recorded while AMPARs were blocked with NBQX (10 μ M), and once equilibrated DL-APV (100 μ M) was applied to the great majority of cells to block and confirm the remaining current as NMDAR-mediated. The amplitudes of NMDAR-mediated currents that were and were not validated by DL-APV application were not significantly different. One neuron was recorded per brain slice, with 1–4 slices recorded per animal.

Streptavidin histochemistry

At the end of some recordings, the pipette was slowly moved away from the cell body and the slice was fixed at least overnight in 4% paraformaldehyde at 4 °C. Slices were then rinsed in phosphate-buffered saline (PBS), blocked in 95% StartingBlock PBS-blocking buffer (ThermoFisher) with 4% PBS and 1% Triton X-100 ("TX", Sigma-Aldrich), rinsed again in 0.25% TX, and then incubated for 1–3 nights at 4 °C in 1% TX/PBS with 1:500 streptavidin conjugated with either Alexa Fluor 488 or 647 (ThermoFisher). Slices were then rinsed in 0.25% TX and mounted using Fluoromount-G (SouthernBiotech). Streptavidin-labeled cell-fills were imaged on a Zeiss LSM 780 confocal microscope using a Plan-Apochromat \times 20, 0.8 numerical aperture objective in Pfizer's Optical Microscopy Technology Center. Alexa Fluor 488 and 647 were excited by corresponding laser lines, and 8-bit images were acquired at \sim 0.35 μ m/voxel in XY and 0.8–2.0 μ m/voxel in Z. Maximum intensity projections shown are from z-stacks processed with ImageJ/Fiji's rolling ball background subtraction algorithm (300-pixel radius) and smoothed with a Gaussian filter (1-pixel radius).

Data analysis

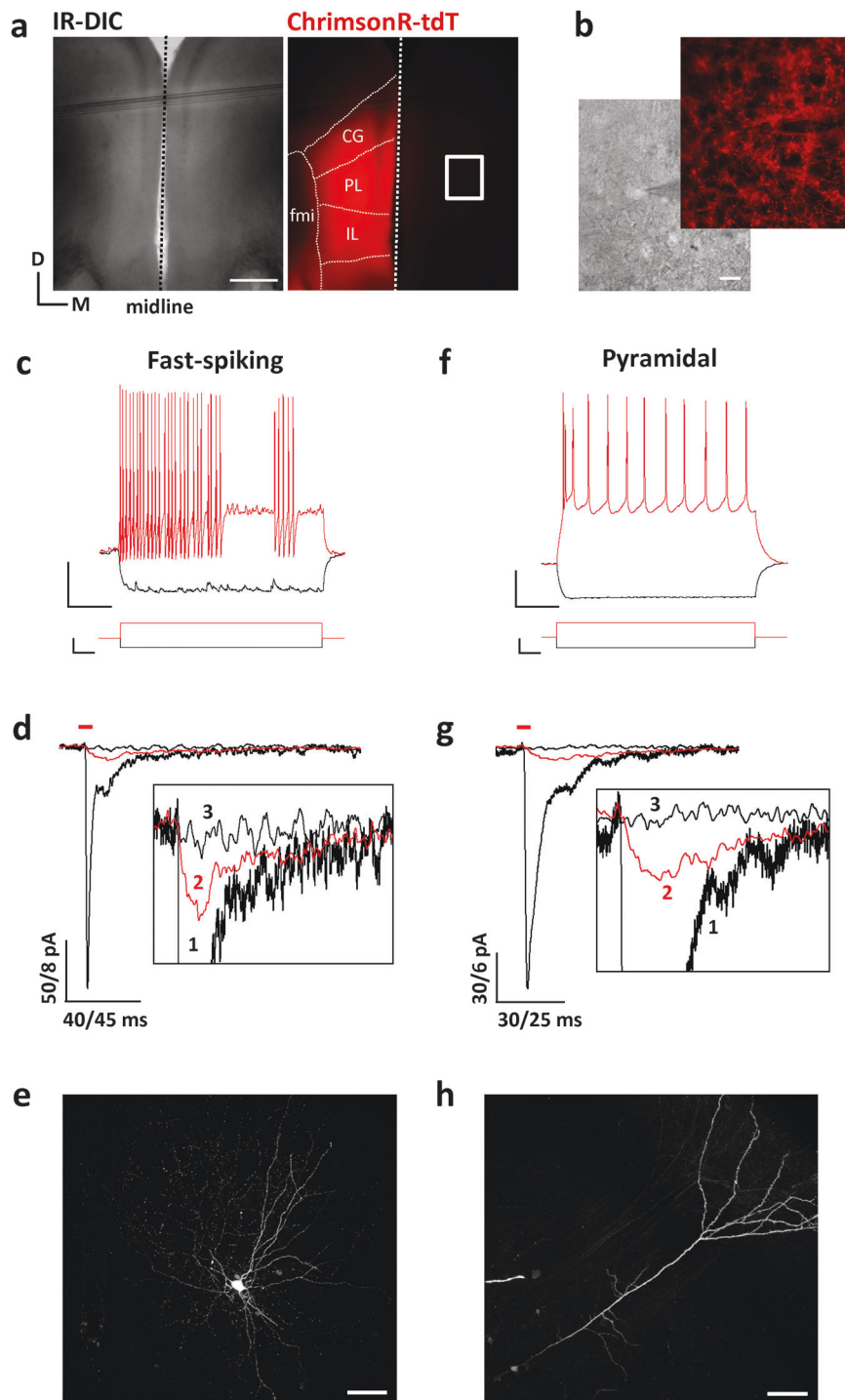
Evoked currents were analyzed using Clampfit, with the last block of sweeps acquired once each drug had equilibrated in the bath (\geq 3 min) before the next drug enters being averaged for subsequent detection and measurement in MiniAnalysis (Synaptosoft Inc.). Additionally, for NBQX and DL-APV average responses, a notch-filter centered on 60 Hz was applied to mitigate line noise, as well as a 300 Hz low-pass Gaussian filter to aid the accurate detection and measurement of small currents. PCX-only responses were not filtered in this manner, as each of the filters shortened the height of the short-duration PCX-only peaks. NMDAR:AMPA ratios were calculated using the peak amplitude of the PCX + NBQX (NMDAR) and PCX-only (AMPA) average responses. Cells whose PCX + NBQX response could not be detected using low-threshold settings in MiniAnalysis (amp \geq 2 pA and area \geq 20) were categorized as "no NMDAR" cells.

Experimental design and statistical analysis

The experiments yielded the following number of data points per input studied: contralateral mPFC (7 animals; 15 FSI and 7 PC); ventral hippocampus (6 animals; 13 FSI and 6 PC); and thalamus (5 animals; 10 FSI and 4 PC). Prism 7 (GraphPad Software Inc.) was used for statistical analyses, and all values reported are mean \pm SEM unless otherwise stated. Significance is summarized in figures as *** P < 0.001. Details of the tests used, comparisons made, and factors analyzed are stated fully in Results.

RESULTS

To investigate input-specific synaptic responses in mPFC FSI, we performed stereotaxic surgeries on adult GAD1-EGFP mice to virally express the red-shifted opsin ChrimsonR in discrete brain regions from which monosynaptic projections to the mPFC are known to originate. We first made unilateral injections of adeno-associated viruses (AAVs) that drive expression of ChrimsonR-tdTomato via the synapsin promoter into the PL and IL areas of



mPFC. After at least 4.5 weeks' recovery time, we prepared acute 300 μm -thick brain slices for *in vitro* physiology and confirmed visually that bulk expression of the tdTomato reporter was restricted to the injected hemisphere (Fig. 1a). In the PL, IL, and CG areas of mPFC in the hemisphere contralateral to the injection, we observed robust labeling of callosally originating axonal processes under high-power magnification (Fig. 1b). We then targeted large, deep-layer GFP+ cells located within this field of tdTomato+ axons for whole-cell recordings. In order to detect the physiological impact of synaptic inputs at the patched soma without artificially boosting space-clamp via a cesium-containing internal solution that blocks potassium channels, we used a

potassium gluconate-based solution to more closely mimic the neuron's native ionic composition. We found that upon somatic injection of supra-threshold current pulses, each of these cells responded with a fast-spiking train of action potentials (red trace, Fig. 1c), consistent with previous reports of GAD1-EGFP mice [18].

We next checked for synaptic connectivity of the patched cell with local ChrimsonR-tdTomato-labeled axons by holding the cell at -55 mV in voltage-clamp and delivering brief, 5 ms flashes of a far-red LED through the objective lenses to the L5/6 region of tissue containing the cell. Cells receiving monosynaptic input from optically-driven axons exhibited a fast-rising inward current

2104 Fig. 1 **a** Coronal section of mouse brain through mPFC (~1.9 mm rostral to bregma), with bulk expression of ChrimsonR-tdTomato in cell bodies restricted to the injected hemisphere, left side in each image. White box indicates L5 region from which high-power image of callosally projecting axons shown in **b** was acquired. Scale bar, 500 μ m. Orientation bar indicates dorsal (D) and medial (M) anatomical directions. CG, cingulate cortex area 1; f.m.i., forceps minor of the corpus callosum; IL, infralimbic cortex; PL, prelimbic cortex. **b** Infrared differential interference contrast image of a patch-clamped FSI (traces shown in **c** and **d**) and corresponding epifluorescence image of callosally originating ChrimsonR-tdTomato-expressing axons in layer 5 of PL mPFC. Epifluorescence image processed with 300-pixel radius rolling-ball background-subtraction algorithm to aid visibility of axons. Scale bar, 20 μ m. **c** Voltage response (top) of an FSI to somatic current injection (bottom) at both sub-threshold (black, -150 pA) and supra-threshold (red, $+250$ pA, 100 pA above rheobase) levels. Scale bars, 20 mV and 100 ms (top), and 200 pA and 50 ms (bottom). **d** Current response of a -55 mV voltage-clamped FSI to light-activation (5 ms, red dash) of local ChrimsonR-tdTomato axons originating in contralateral mPFC. Inset, larger view of the effects of sequentially applied drugs on average current responses: (1) picrotoxin [10 μ M], to block GABA_A-receptor-mediated inhibition and isolate excitatory currents; (2) red trace, NBQX [10 μ M], to block AMPAR-mediated current and isolate NMDAR-mediated component; (3) DL-APV [100 μ M], to extinguish NMDAR-mediated current. Scale bar applies to both overview (first number) and inset (second number). **e** Maximum intensity projection of a confocal image stack of a fluorescent streptavidin-labeled example FSI, not from this brain. Pial surface is toward the upper right. Scale bar, 50 μ m. **f, g** Same as in **c** and **d**, but for a pyramidal cell recorded in another slice of the brain shown in **a**. Supra-threshold voltage response shown is to 200 pA current injection, also 100 pA above rheobase. **h** Same as in **e**, but for a pyramidal cell from a different brain. Scale bar, 50 μ m

response that peaked within milliseconds of stimulation (Fig. 1d). After blocking GABA_A-receptor-mediated inhibition with picrotoxin (10 μ M), the stimulus intensity was titrated to obtain the largest EPSC that did not lead the cell to spike (black trace #1, Fig. 1d). Baseline responses were recorded for several minutes at a 30-s inter-stimulus interval, and then NBQX (10 μ M) was added to the bath to block AMPA-type glutamate receptors. Following equilibration of NBQX, an isolated NMDAR-mediated current of 8.2 ± 1.1 pA peak amplitude was observable in most FSI (red trace, Fig. 1d). In order to measure the amplitude of NMDAR current that a cell would experience in native conditions, these recordings were made with 1 mM Mg²⁺ in the ACSF. These NMDAR-mediated currents had a rise time of 6.9 ± 1 vs. 1.8 ± 0.1 ms for the AMPAR-dominated component, and were extinguished by application of DL-APV (100 μ M; black trace #3, Fig. 1d). Following some experiments, we fixed the brain slice with paraformaldehyde and then performed streptavidin histochemistry to label neurobiotin that diffused into the cell from the recording pipette. Confocal imaging of these filled cells allowed for morphological confirmation of cell type, with GFP+ FSI exhibiting multipolar cell bodies and local, highly branched axons (Fig. 1e) [18].

In addition to GFP+ FSI, we also targeted deep-layer PCs and classified them via membrane properties as putative “type A” (thick-tufted and subcortically-projecting) or “type B” (thin-tufted and callosally-projecting) cells [11]. In total, ~70% of our sample lacked a hyperpolarizing sag in the voltage response to onset of negative current injection (black trace, Fig. 1f), lacked rebound-depolarization upon injection completion, and did not exhibit an overshooting after-hyperpolarization following spiking (red trace, Fig. 1f), signaling their identity as type B cells. We performed identical synaptic physiology experiments on PCs, finding a peak amplitude of 13.3 ± 4.1 pA NMDAR-mediated current with 8.5 ± 1.4 ms rise time, vs. 2.6 ± 0.4 ms for AMPAR (Fig. 1g). As for FSI, neurobiotin fills of physiologically-identified PCs provided for morphological confirmation of cell type via observation of the apical dendrite (Fig. 1h).

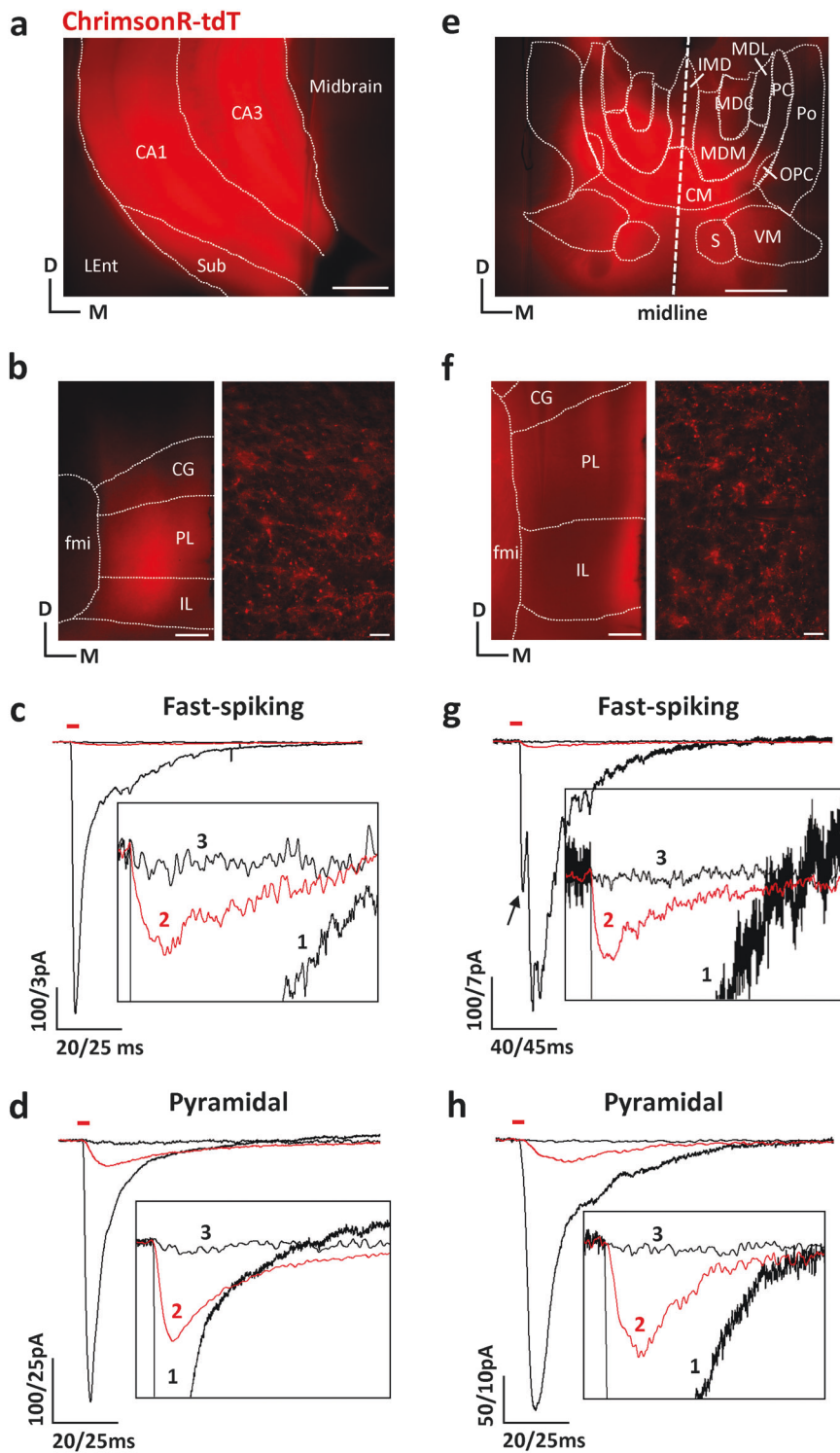
We also investigated projection-specific responses of FSI and PCs to optogenetic activation of ventral hippocampal (Fig. 2a–d) and thalamic (Fig. 2e–h) inputs to mPFC. Following bilateral injection of AAVs encoding ChrimsonR-tdTomato into ventral CA1 and subiculum, we observed strong, localized expression in the target region (Fig. 2a) and in projections centered on PL mPFC (Fig. 2b, left). Similar to deep-layer regions targeted by axons originating from contralateral mPFC, we observed dense ventral hippocampal inputs in L5 (Fig. 2b, right). Upon voltage-clamping GFP+ FSI at -55 mV and activating local hippocampal axons with red light flashes in the presence of PCX, we also observed large, fast-rising AMPAR-dominated inward currents (black trace #1, Fig. 2c). With NBQX onboard to block these receptors (red trace, Fig. 2c), a distinct, albeit low-amplitude NMDAR-mediated

component was revealed in FSI (5.2 ± 0.5 pA peak amplitude, rise time of 6.6 ± 1.3 vs. 2.0 ± 0.2 ms for AMPAR), as it was in cells activated by inputs from contralateral mPFC. Similarly, PCs activated by hippocampal inputs also showed NMDAR-mediated responses (16.7 ± 6.2 pA peak amplitude, rise time of 8.2 ± 1.4 vs. 3.4 ± 0.3 ms for AMPAR, Fig. 2d).

Thalamic injections were targeted to the mediodorsal nucleus, with the bulk of the resulting labeling centered on midbrain areas ~1.3 mm caudal to bregma and slightly posterior. Nuclei in the vicinity of the mediodorsal nucleus were also labeled in most animals (Fig. 2e), and the better-labeled hemisphere was chosen for recordings. Projections to mPFC showed a stereotypical pattern of labeling in which layer 1 was brightest (Fig. 2f, left), and layer 5 possessed an axonal density similar to the other inputs studied (Fig. 2f, right). Innervated GFP+ FSI showed rapid and strong responses following optogenetic activation of thalamus-originating axons (Fig. 2g). Because these responses often featured a prominent polysynaptic component, we were careful to identify the initial, monosynaptic peak (arrow, Fig. 2g) in order to restrict our analyses to the first-order effects of activating thalamic axons specifically. As with other inputs, pharmacologically isolated NMDAR-mediated currents were clearly evident in recorded FSI (8.7 ± 1.4 pA peak amplitude, with rise time of 8.7 ± 1.5 vs. 2.2 ± 0.2 ms for AMPAR), and were extinguished by application of DL-APV. PCs in layer 5 of mPFC were similarly well-innervated by thalamic axons, the activation of which evoked sizable NMDAR-mediated currents in these cells (26.1 ± 6.6 pA peak amplitude, with rise time of 13.7 ± 0.6 vs. 4.8 ± 0.4 ms for AMPAR, Fig. 2h).

The vast majority of FSI we recorded exhibited NMDAR currents in response to activation of axons belonging to specific afferent pathways to the mPFC ($n = 34/38$, Fig. 3a). NMDAR currents were universally present in recordings from L5 pyramidal neurons ($n = 17/17$). FSI lacking NMDAR responses were equally distributed between groups on the basis of input studied (Fig. 3a). Across all inputs, the peak amplitude of the raw NMDAR currents recorded in FSI ranged from ~2.5–17 pA (average 7.26 ± 3.67 pA, SD; Fig. 3b), and in PCs from ~3.5–43 pA overall (average 17.5 ± 13.3 pA, SD). In a two-way analysis of variance (ANOVA) there was a main effect of cell type ($F_{(1,45)} = 22.7$, $P < 0.0001$) indicating that PCs exhibited significantly larger responses than did FSI, but only a trend toward an effect of input ($F_{(2,45)} = 2.9$, $P = 0.0651$; interaction: $F_{(2,45)} = 2.2$, $P = 0.1254$).

Importantly, the peak current that we observed before isolating NMDAR currents (i.e., AMPAR-dominated) varied from cell to cell (Fig. 3c), as expected due to variability in the efficiency of viral infections arising across animals injected, pathways stimulated, and slices recorded. Specifically, while there was only a trend toward increased peak AMPAR currents being observed in FSI vs. PCs (two-way ANOVA, cell type: $F_{(1,49)} = 3.3$, $P = 0.0775$; input:



$F_{(2,49)} = 0.5$, $P = 0.598$; interaction: $F_{(2,49)} = 3.1$, $P = 0.0555$), using each cell's AMPAR amplitude to normalize the amount of NMDAR-mediated current recorded in the same cell controls for the number of active synapses when comparing across cells. This revealed that FSI had a significantly smaller NMDAR:AMPA ratio than did PCs (two-way ANOVA, cell type: $F_{(1,45)} = 70.8$, $P < 0.0001$; Fig. 3d), and that there was also a main effect of input-studied ($F_{(2,45)} = 5.7$, $P = 0.0062$; interaction: $F_{(2,45)} = 0.5$, $P = 0.6137$).

Considering the absolute NMDAR-mediated response, the area under the curve of these currents was significantly smaller for FSI

than it was for PCs (two-way ANOVA, cell type: $F_{(1,45)} = 14$, $P = 0.0005$; input: $F_{(2,45)} = 2.1$, $P = 0.1318$; interaction: $F_{(2,45)} = 2.1$, $P = 0.1341$; Fig. 3e). Additionally, as the time-course of synaptically driven NMDAR responses can influence FSI ability to integrate inputs, we tested whether there were cell type- and input-specific differences in this parameter. When we measured time to decay of the NMDAR-mediated current to 5% of peak amplitude, it did not differ between cell type or input studied (two-way ANOVA, cell type: $F_{(1,45)} = 1.2$, $P = 0.2698$; input: $F_{(2,45)} = 0.2$, $P = 0.854$; interaction: $F_{(2,45)} = 0.1$, $P = 0.8699$; Fig. 3f).

2106 Fig. 2 **a** Epifluorescence image of coronal section through ventral hippocampus (~3.4 mm caudal to bregma), with expression of ChrimsonR-tdTomato restricted to the target structure. Scale bar, 500 μm . Orientation bar, dorsal (D) and medial (M) directions. CA1, field CA1 of hippocampus; CA3, field CA3 of hippocampus; LEnt, lateral entorhinal cortex; Sub, subiculum. **b** Left, epifluorescence image of projections to mPFC from the ChrimsonR-tdTomato-labeled hippocampus shown in **a**, with the right-hand side of the image bordering the medial pial surface. Image processed with 100-pixel radius algorithm to aid visibility of projections. Structures labeled as in Fig. 1a. Scale bar, 200 μm . Right, example image of hippocampally-originating ChrimsonR-tdTomato-labeled axons in layer 5 of PL mPFC. Image processed with 300-pixel radius algorithm. Scale bar, 20 μm . **c** Current response of a -55 mV voltage-clamped FSI to light-activation (5 ms, red dash) of local ChrimsonR-tdTomato axons originating in the hippocampus. Inset and scale bar as in Fig. 1d. Average trace #1, picrotoxin-only, was additionally low-pass filtered at 1 kHz in the inset to remove a noise transient, visible ~40 ms into the overview trace at the top. **d** Same as in **c**, but for a pyramidal cell light-activated by hippocampal inputs. **e** Epifluorescence image of coronal section through mediodorsal thalamic nuclei (~1.7 mm caudal to bregma), with lower levels of ChrimsonR-tdTomato expression also present in adjacent structures. Scale bar, 500 μm . MDC mediodorsal thalamic nucleus, central; MDL mediodorsal thalamic nucleus, lateral; MDM mediodorsal thalamic nucleus, medial; CM central medial thalamic nucleus; IMD intermediodorsal thalamic nucleus; OPC oval paracentral thalamic nucleus; PC paracentral thalamic nucleus; Po posterior thalamic nuclear group; S submedius thalamic nucleus; VM ventromedial thalamic nucleus. **f** Left, epifluorescence image of mPFC ipsilateral to the left-hand side of the ChrimsonR-tdTomato-labeled thalamus shown in **e**, with prominent projections to layer 1 visible medially on the right-hand side. The pipette from the deep-layer recording shown in **g** is visible entering from the top of the image. Scale bar, 200 μm . Right, example image of thalamically-originating ChrimsonR-tdTomato-labeled axons in layer 5 of mPFC. Scale bar, 20 μm . Structures labeled as in Fig. 1a. **g, h** Same as in **c** and **d**, for an FSI and a pyramidal cell, respectively, that were light-activated by thalamically-originating axons from the brain shown in **e**. The arrowhead in **g** indicates the monosynaptic component from which peak AMPAR-mediated current was measured

DISCUSSION

We assessed NMDAR-mediated currents evoked by projection-specific optogenetic activation of contralateral mPFC, hippocampal, and thalamic inputs to FSI and pyramidal neurons in deep-layer mPFC of adult male mice. Activation of each of these long-range inputs led to NMDAR responses in the vast majority of FSI recorded, independently of which input was activated, and in all PCs. Accounting for differential activation of cells by considering the ratio of NMDAR to AMPAR peak currents, FSI had a smaller NMDAR:AMPA ratio than did PCs, whose ratio for a given input was two- to fourfold greater.

We were likely underestimating NMDAR currents in these experiments, as our recordings were performed in ACSF with 1 mM Mg^{2+} and cells were voltage-clamped at -55 mV in the presence of NBQX. Thus, attenuation of AMPAR-mediated depolarization would reduce depolarization-dependent components in the NMDAR response. NMDAR-mediated EPSCs recorded in FSI exhibit a current-voltage curve that is depolarization-shifted compared to that seen in PCs [19], indicating that currents recorded in FSI at a given negative potential are smaller relative to those recorded in PCs. Indeed, FSI demonstrate robust NMDAR-mediated currents at positive potentials [19], including in adult mPFC [20]. NMDAR have also been found to mediate the bulk of calcium entry into FSI dendrites during synaptic activity, with their recruitment reliant upon activation of AMPAR [21]. It is also likely that the space-clamp afforded by our potassium-gluconate internal did not extend to the distal dendrites [22], from which attenuation of EPSPs is evident in somatic recordings of hippocampal FSI [23] and L5 PCs [22], including their basal dendrites [24]. Although dendrites of neocortical FSI can extend over 200 μm from the soma and receive excitatory inputs until they terminate, relatively little is known about the precise localization of distinct long-range afferents, beyond the presence of thalamic inputs throughout the somatodendritic region of even L5 FSI [25]. However, joint somatic and apical dendritic recordings have revealed that most L5 PCs in mPFC receive callosal input to both compartments, with hippocampal inputs interestingly more prevalent and stronger onto type B somata and dendrites than onto type A PCs [26]. While we lack the numbers to address input selectivity among PC subtypes, that to the extent known each input we studied makes perisomatic contacts suggests that our somatic recordings largely comprised proximally-originating events [22]. Additionally, it is unlikely that the currents we recorded reflect substantial activation of extrasynaptic NMDAR receptors [27], as our lab has found that blockade of glutamate transporters is needed to promote spillover of glutamate outside of the synapse following brief activation of local inputs to FSI in adult rat mPFC (Lewis and O'Donnell, unpublished observations).

Thus, our data indicate that FSI do exhibit measurable NMDAR currents even in biophysically limited conditions that are close to the physiological *in vivo* setting.

Our results largely agree with those of previous studies [6], namely that NMDAR-mediated currents, while small, are present in FSI in adult mPFC. Using optogenetics, we observed NMDAR-mediated currents in a higher proportion of FSI ($n = 34$ of 38) than was seen by Wang and Gao [20] in adult rat mPFC, who recorded EPSCs evoked by electrical stimulation in L2/3 and found that only 6 of 23 cells exhibited NMDAR responses. In addition to differences in species (mouse vs. rat), mPFC subregion (IL, PL, and CG vs. PL), and layer recorded (deep layers, mainly L5 vs. all layers, largest proportion in L2/3), differences in stimulation paradigm may also play a role. Our optogenetic activation of inputs to a given cell was restricted to a single population of afferent fibers, which is more likely to yield homogeneous responses. Local electrical stimulation likely activates a diverse set of inputs, including recurrent intracortical synapses, which may activate NMDAR differently than the long-range inputs that we studied. Indeed, input-specific differences in NMDAR-subunit composition have been observed at callosal vs. intracortical synapses onto layer 5 PCs in frontal cortex [28], raising the possibility that such differences may exist on the receptor-level for these and other inputs to FSI.

Our finding that multiple long-range inputs to mPFC can evoke NMDAR responses in a high proportion of FSI—an apparent contrast to intracortical inputs [20]—highlights the notion that FSI dysfunction in schizophrenia [1] and NMDAR-antagonism models of the disease [3] need to be considered in a global rather than local context of mPFC circuitry. For instance, recent work has begun to elucidate the impact of excitatory inputs from mediodorsal thalamus on mPFC networks. Feedforward inhibition, as dissected in sensory cortices [29] and described for other inputs to mPFC such as hippocampus [12], is mediated by rapid activation of FSI, whose subsequent inhibitory output onto PCs defines these cells' temporal window of integration to reach spike threshold. Delevich et al. [30] have detailed the mechanisms of feedforward inhibition governing mediodorsal-thalamic input to mPFC, which interestingly lacks several of the features common among sensory thalamocortical pathways, such as stronger synapses onto FSI vs. PCs and an ultra-short lag between excitation and the onset of disinaptic, FSI-mediated inhibition (~4.8 vs. 1–3 ms in sensory areas). Given the absence of these specializations, longer-duration NMDAR-mediated currents may be especially important in regulating thalamocortical activation of mPFC FSI, ultimately influencing their efficacy at gating thalamic and even hippocampal [31] activation of broader mPFC networks. Further, as nearly all of the FSI we recorded exhibited NMDAR

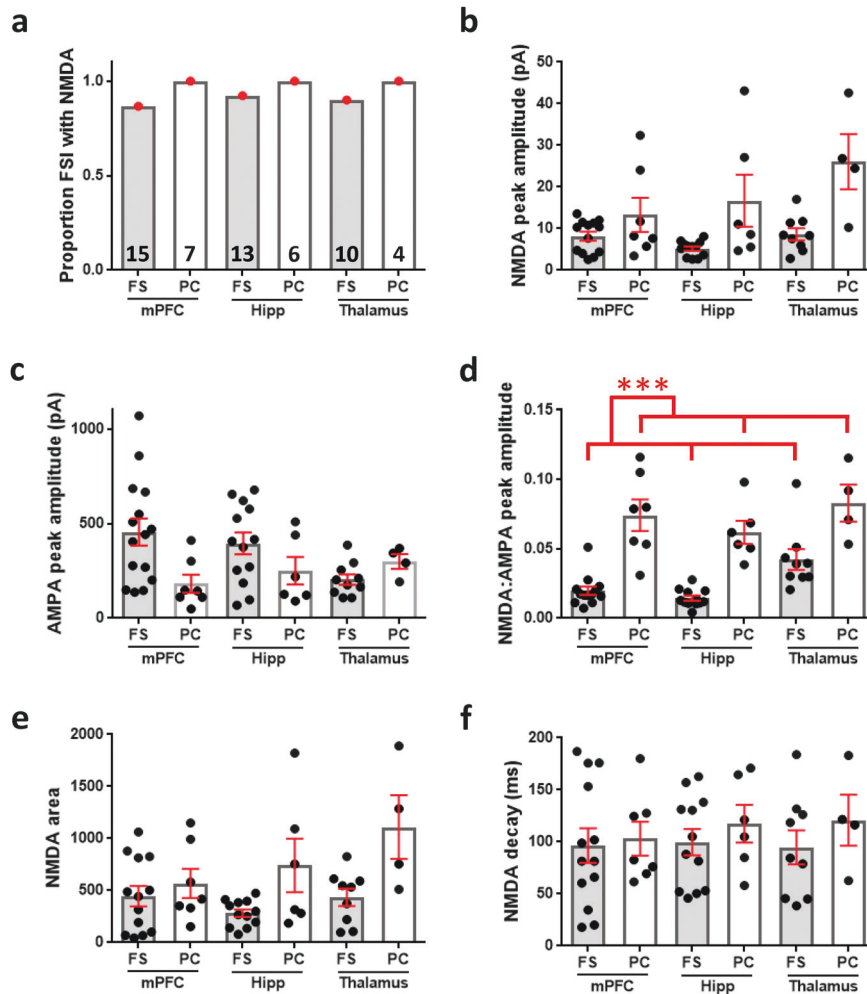


Fig. 3 **a** The proportion of FSI and pyramidal neurons activated by each input tested that exhibited a detectable NMDAR-mediated current. The total number of cells recorded per condition is indicated at the bottom of each bar. **b** Peak amplitude of NMDAR-mediated current recorded in cells activated by a given input (two-way ANOVA, cell type: $F_{(1,45)} = 22.7$, $P < 0.0001$; input: $F_{(2,45)} = 2.9$, $P = 0.0651$; interaction: $F_{(2,45)} = 2.2$, $P = 0.1254$). All error bars indicate SEM. **c** Peak amplitude of AMPAR-dominated current recorded in cells that demonstrated a detectable NMDAR-mediated current (two-way ANOVA, cell type: $F_{(1,49)} = 3.3$, $P = 0.0775$; input: $F_{(2,49)} = 0.5$, $P = 0.598$; interaction: $F_{(2,49)} = 3.1$, $P = 0.0555$). **d** Ratio of the peak amplitude of NMDAR-mediated current (NBQX and picrotoxin onboard) to AMPAR-dominated current (picrotoxin only). Asterisks indicate main effect of cell type ($F_{(1,45)} = 70.8$, $P < 0.0001$) in two-way ANOVA (input: $F_{(2,45)} = 5.7$, $P = 0.0062$; interaction: $F_{(2,45)} = 0.5$, $P = 0.6137$). **e** Area under the curve of NMDAR-mediated currents recorded in cells activated by a given input, smaller for FSI than for PCs (two-way ANOVA, cell type: $F_{(1,45)} = 14$, $P = 0.0005$; input: $F_{(2,45)} = 2.1$, $P = 0.1318$; interaction: $F_{(2,45)} = 2.1$, $P = 0.1341$). **f** Time to decay of NMDAR-mediated current to 5% of peak amplitude (two-way ANOVA, cell type: $F_{(1,45)} = 1.2$, $P = 0.2698$; input: $F_{(2,45)} = 0.2$, $P = 0.854$; interaction: $F_{(2,45)} = 0.1$, $P = 0.8699$)

currents in response to activation of the one class of input tested per cell, it is likely that each FSI receives convergent input from all three sources studied. The functional impact of this convergence onto interneurons mediating feedforward inhibition awaits further study, and could be dissected with pairwise, pathway-specific activation using multiple, independently excitable opsins [15].

Once recruited by long-range afferents, feedforward inhibitory networks drive gamma-oscillations in which ensembles of neurons spike in synchrony at roughly 40 Hz. Gamma activity is thought to reflect integration of information across brain regions and other processes that underlie cognition and memory, and schizophrenia patients fail to exhibit increases in gamma-power typically seen during tasks utilizing these abilities [1]. Interestingly, while mice lacking NMDAR selectively in FSI (PV-Cre/NR1^{fl/fl}) [32] show an increase in PFC baseline gamma, they also show a reduction in task-evoked gamma, similar to schizophrenia patients. One difference in brain state between baseline and task-evoked conditions is a likely higher level of phasic activity in long-range

inputs to PFC during task performance, which would normally engage feedforward inhibition more efficiently due to synchronous activation of the FSI network [33–35], elevating gamma oscillations. Without activation of FSI aided by NMDAR [32], afferents may show diminished efficacy in recruiting feedforward inhibition or sustaining its engagement even during tasks, thereby failing to increase gamma activity. FSI are also electrically coupled to one another by gap junctions [36], intercellular pores with low-pass filtering properties optimized to conduct charge from slow NMDAR currents rather than quickly decaying AMPAR currents and action potentials. Without functional NMDAR, FSI are unlikely to fully leverage electrical coupling's potential to spread excitability between connected cells and promote robust activation of feedforward inhibitory networks.

Growing evidence suggests that an important effect of NMDAR antagonism is perturbation of intrinsic activity in brain regions upstream of mPFC such as mediodorsal thalamus [37] and ventral hippocampus [38], whose projections in turn contribute to over-

2108 activation of mPFC networks and resultant symptomatology. Together with our data indicating the presence of NMDAR at synapses formed by these projections onto FSI, a reevaluation of mPFC-centric models of NMDAR hypofunction is needed. Not only should a potential role of NMDAR antagonists on FSI not be discarded as relevant to schizophrenia pathophysiology, but our data indicate that long-range connectivity deficits may play a role in driving an NMDAR hypofunction-dependent interneuron deficit in schizophrenia and related conditions.

ACKNOWLEDGEMENTS

We thank K. Hales for assistance with confocal imaging, J. Brooks, J. Thompson, & S. Gee for technical advice, and all members of the O'Donnell lab for their feedback.

FUNDING

LJB and PO are/were employees and stockholders of Pfizer, Inc., which funded this basic research project inspired by Pfizer's interest in developing novel treatments for psychiatric disease. This manuscript does not include use of any proprietary reagents. PO is currently an employee of Takeda Pharmaceuticals.

ADDITIONAL INFORMATION

Competing interests: The authors declare no competing interests.

Publisher's note: Springer Nature remains neutral with regard to jurisdictional claims in published maps and institutional affiliations.

REFERENCES

1. Lewis DA, Curley AA, Glausier JR, Volk DW. Cortical parvalbumin interneurons and cognitive dysfunction in schizophrenia. *Trends Neurosci.* 2012;35:57–67.
2. Javitt DC, Zukin SR. Recent advances in the phencyclidine model of schizophrenia. *Am J Psychiatry.* 1991;148:1301–8.
3. Homayoun H, Moghaddam B. NMDA receptor hypofunction produces opposite effects on prefrontal cortex interneurons and pyramidal neurons. *J Neurosci.* 2007;27:11496–500.
4. Marin O. Interneuron dysfunction in psychiatric disorders. *Nat Rev Neurosci.* 2012;13:107–20.
5. Rudy B, Fishell G, Lee S, Hjerling-Leffler J. Three groups of interneurons account for nearly 100% of neocortical GABAergic neurons. *Dev Neurobiol.* 2011;71:45–61.
6. Rotaru DC, Yoshino H, Lewis DA, Ermentrout GB, Gonzalez-Burgos G. Glutamate receptor subtypes mediating synaptic activation of prefrontal cortex neurons: relevance for schizophrenia. *J Neurosci.* 2011;31:142–56.
7. Kochunov P, Hong LE. Neurodevelopmental and neurodegenerative models of schizophrenia: white matter at the center stage. *Schizophr Bull.* 2014;40:721–8.
8. Kochunov P, Ganjgahi H, Winkler A, Kelly S, Shukla DK, Du X, et al. Heterochronicity of white matter development and aging explains regional patient control differences in schizophrenia. *Hum Brain Mapp.* 2016;37:4673–88.
9. Meyer-Lindenberg AS, Olsen RK, Kohn PD, Brown T, Egan MF, Weinberger DR, et al. Regionally specific disturbance of dorsolateral prefrontal-hippocampal functional connectivity in schizophrenia. *Arch Gen Psychiatry.* 2005;62:379–86.
10. Woodward ND, Karbasforoushan H, Heckers S. Thalamocortical dysconnectivity in schizophrenia. *Am J Psychiatry.* 2012;169:1092–9.
11. Lee AT, Gee SM, Vogt D, Patel T, Rubenstein JL, Sohal VS. Pyramidal neurons in prefrontal cortex receive subtype-specific forms of excitation and inhibition. *Neuron.* 2014;81:61–8.
12. Tierney PL, Degenetais E, Thierry AM, Glowinski J, Gioanni Y. Influence of the hippocampus on interneurons of the rat prefrontal cortex. *Eur J Neurosci.* 2004;20:514–24.
13. Alcaraz F, Marchand AR, Courtand G, Coutureau E, Wolff M. Parallel inputs from the mediadorsal thalamus to the prefrontal cortex in the rat. *Eur J Neurosci.* 2016;44:1972–86.
14. Gigg J, Tan AM, Finch DM. Glutamatergic hippocampal formation projections to prefrontal cortex in the rat are regulated by GABAergic inhibition and show

convergence with glutamatergic projections from the limbic thalamus. *Hippocampus.* 1994;4:189–98.

15. Klapoetke NC, Murata Y, Kim SS, Pulver SR, Birdsey-Benson A, Cho YK, et al. Independent optical excitation of distinct neural populations. *Nat Methods.* 2014;11:338–46.
16. Tseng KY, O'Donnell P. Dopamine modulation of prefrontal cortical interneurons changes during adolescence. *Cereb Cortex.* 2007;17:1235–40.
17. Paxinos G, Franklin KBJ (2001). *The Mouse Brain in Stereotaxic Coordinates*, 2nd edn. Academic Press.
18. Chattopadhyaya B, Di Cristo G, Higashiyama H, Knott GW, Kuhlman SJ, Welker E, et al. Experience and activity-dependent maturation of perisomatic GABAergic innervation in primary visual cortex during a postnatal critical period. *J Neurosci.* 2004;24:9598–11.
19. Hull C, Isaacson JS, Scanziani M. Postsynaptic mechanisms govern the differential excitation of cortical neurons by thalamic inputs. *J Neurosci.* 2009;29:9127–36.
20. Wang HX, Gao WJ. Cell type-specific development of NMDA receptors in the interneurons of rat prefrontal cortex. *Neuropsychopharmacology.* 2009;34:2028–40.
21. Goldberg JH, Yuste R, Tamas G. Ca²⁺-imaging of mouse neocortical interneurone dendrites: contribution of Ca²⁺-permeable AMPA and NMDA receptors to sub-threshold Ca²⁺-dynamics. *J Physiol.* 2003;551:67–78.
22. Williams SR, Mitchell SJ. Direct measurement of somatic voltage clamp errors in central neurons. *Nat Neurosci.* 2008;11:790–98.
23. Norenberg A, Hu H, Vida I, Bartos M, Jonas P. Distinct nonuniform cable properties optimize rapid and efficient activation of fast-spiking GABAergic interneurons. *Proc Natl Acad Sci USA.* 2010;107:894–9.
24. Nevian T, Larkum ME, Polsky A, Schiller J. Properties of basal dendrites of layer 5 pyramidal neurons: a direct patch-clamp recording study. *Nat Neurosci.* 2007;10:206–14.
25. Kameda H, Hioki H, Tanaka YH, Tanaka T, Sohn J, Sonomura T, et al. Parvalbumin-producing cortical interneurons receive inhibitory inputs on proximal portions and cortical excitatory inputs on distal dendrites. *Eur J Neurosci.* 2012;35:838–54.
26. Dembrow NC, Zemelman BV, Johnston D. Temporal dynamics of L5 dendrites in medial prefrontal cortex regulate integration versus coincidence detection of afferent inputs. *J Neurosci.* 2015;35:4501–14.
27. Povysheva NV, Johnson JW. Tonic NMDA receptor-mediated current in prefrontal cortical pyramidal cells and fast-spiking interneurons. *J Neurophysiol.* 2012;107:2232–43.
28. Kumar SS, Huguenard JR. Pathway-specific differences in subunit composition of synaptic NMDA receptors on pyramidal neurons in neocortex. *J Neurosci.* 2003;23:10074–83.
29. Cruikshank SJ, Lewis TJ, Connors BW. Synaptic basis for intense thalamocortical activation of feedforward inhibitory cells in neocortex. *Nat Neurosci.* 2007;10:462–68.
30. Delevich K, Tucciarone J, Huang ZJ, Li B. The mediadorsal thalamus drives feedforward inhibition in the anterior cingulate cortex via parvalbumin interneurons. *J Neurosci.* 2015;35:5743–53.
31. Floresco SB, Grace AA. Gating of hippocampal-evoked activity in prefrontal cortical neurons by inputs from the mediadorsal thalamus and ventral tegmental area. *J Neurosci.* 2003;23:3930–43.
32. Carlen M, Meletis K, Siegle JH, Cardin JA, Futai K, Vierling-Claassen D, et al. A critical role for NMDA receptors in parvalbumin interneurons for gamma rhythm induction and behavior. *Mol Psychiatry.* 2012;17:537–48.
33. Hensch TK. Critical period plasticity in local cortical circuits. *Nat Rev Neurosci.* 2005;6:877–88.
34. Kuhlman SJ, Lu J, Lazarus MS, Huang ZJ. Maturation of GABAergic inhibition promotes strengthening of temporally coherent inputs among convergent pathways. *PLoS Comput Biol.* 2010;6:e1000797.
35. Galarreta M, Hestrin S. Spike transmission and synchrony detection in networks of GABAergic interneurons. *Science.* 2001;292:2295–9.
36. Galarreta M, Hestrin S. Electrical and chemical synapses among parvalbumin fast-spiking GABAergic interneurons in adult mouse neocortex. *Proc Natl Acad Sci USA.* 2002;99:12438–43.
37. Kiss T, Hoffmann WE, Scott L, Kawabe TT, Milici AJ, Nilsen EA, et al. Role of thalamic projection in NMDA receptor-induced disruption of cortical slow oscillation and short-term plasticity. *Front Psychiatry.* 2011;2:14.
38. Jodo E. The role of the hippocampo-prefrontal cortex system in phencyclidine-induced psychosis: a model for schizophrenia. *J Physiol Paris.* 2013;107:434–40.